Controlling charge density order in 2*H*-$TaSe_2$ using a van Hove singularity

W. R. B. Luckin,[1,*] Y. Li,[2,3,*,†] J. Jiang,[4] S. M. Gunasekera,[1] C. Wen,[3] Y. Zhang,[3] D. Prabhakaran,[5] F. Flicker,[6] Y. Chen,[5,3,7] and M. Mucha-Kruczyński[1,8,‡]

[1]*Department of Physics, University of Bath, Claverton Down, Bath BA2 7AY, United Kingdom*
[2]*Institute for Advanced Studies (IAS), Wuhan University, Wuhan 430072, People's Republic of China*
[3]*School of Physical Science and Technology, ShanghaiTech University, Shanghai 201210, People's Republic of China*
[4]*School of Emerging Technology, University of Science and Technology of China, Hefei 230026, People's Republic of China*
[5]*Department of Physics, University of Oxford, Oxford, OX1 3PU, United Kingdom*
[6]*School of Physics and Astronomy, Cardiff University, Cardiff CF24 3AA, United Kingdom*
[7]*CAS-Shanghai Science Research Center, Shanghai 201210, People's Republic of China*
[8]*Centre for Nanoscience and Nanotechnology, University of Bath, Claverton Down, Bath BA2 7AY, United Kingdom*

(Received 4 November 2022; revised 29 November 2023; accepted 4 December 2023; published 24 January 2024)

We report on the interplay between a van Hove singularity and a charge density wave state in 2*H*-$TaSe_2$. We use angle-resolved photoemission spectroscopy to investigate changes in the Fermi surface of this material under surface doping with potassium. At high doping, we observe modifications which imply the disappearance of the (3×3) charge density wave and formation of a different correlated state. Using a tight-binding-based approach as well as an effective model, we explain our observations as a consequence of coupling between the single-particle Lifshitz transition during which the Fermi level passes a van Hove singularity and the charge density order. In this scenario, the high electronic density of states associated with the van Hove singularity induces a change in the periodicity of the charge density wave from the known (3×3) to a new (2×2) superlattice.

DOI: 10.1103/PhysRevResearch.6.013088

I. INTRODUCTION

Because of the fundamental importance of the electrons in the vicinity of the Fermi surface (FS) for low-energy excitations, the shape of this surface has a significant impact on the properties of metals [1]. This is particularly evident when, as a function of some external parameter like pressure [2–4], temperature [5–7], magnetic field [8–10], or doping [11–13], the FS undergoes a change of topology, resulting in a Lifshitz transition (also known as electronic topological transition) [14]. In contrast to the more conventional phase transitions described by the Landau theory, Lifshitz transitions do not involve symmetry breaking but still lead to singularities in many observables [15], because changes of topology of the equi-energetic surface are accompanied by van Hove singularities in the electronic density of states (DoS).

The impact of van Hove singularities is especially significant in low dimensions, $d \leqslant 2$, where divergences in the DoS are possible at some of the dispersion critical points. This is the case for saddle points for $d = 2$ which lead to a logarithmic divergence in the DoS [16,17], the presence of which is often implicated in promoting new orders in two-dimensional and layered materials [18–34], including high-temperature superconducting cuprates [18,23,24], topological kagome superconductors [25–28], and magic-angle twisted bilayer graphene and other graphene materials [29–34].

Here, we study the impact of a Lifshitz transition and the associated van Hove singularity on a charge density wave (CDW)—a correlated ordering of electrons which form a standing-wave pattern accompanied by a periodic distortion of the atomic lattice—by surface doping bulk 2*H*-$TaSe_2$ with potassium. Using angle-resolved photoemission spectroscopy (ARPES), we map out directly the electronic dispersion in its low-temperature commensurate (3×3) CDW, that is, one with a superstructure described by tripling of the in-plane primitive lattice vectors of the uncorrelated state. We then observe how it changes as the previously unoccupied electronic states in the topmost layers are filled so that the chemical potential crosses a saddle point in the dispersion. Based on calculations of generalized susceptibility within a minimal two-band model and effective description of the coupling between the saddle points, we conclude that the change in FS topology drives a change in the CDW from a (3×3) to a (2×2) order. Such a scenario supports a theoretical prediction from almost half a century ago [20] that suggested involvement of the van Hove singularities in the formation of the CDW in $TaSe_2$ but was later shown not to be relevant for the (3×3) phase. It also demonstrates the potential of engineering many-body phases using van Hove singularities.

*These authors contributed equally to this work.
†yiweili@whu.edu.cn
‡M.Mucha-Kruczynski@bath.ac.uk

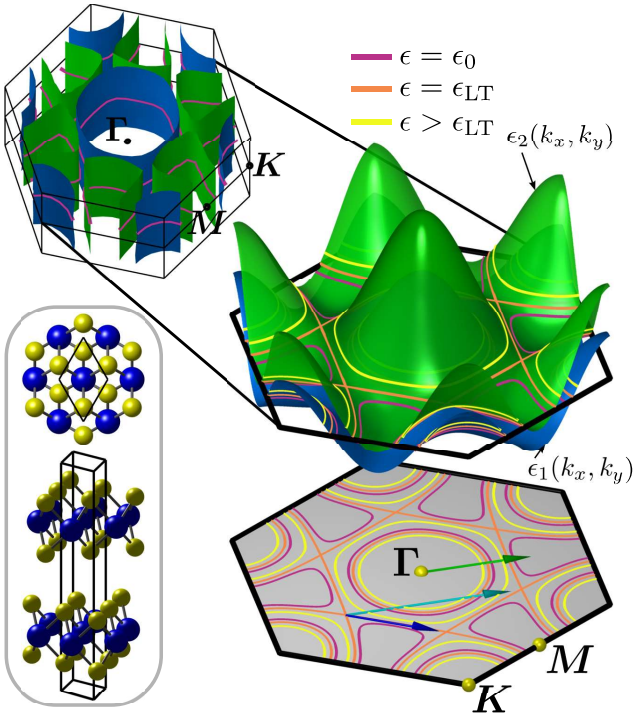

FIG. 1. Dispersion and topology of electronic bands of 2*H*-$TaSe_2$. In the top left, the quasi-2D Fermi surface of undoped 2*H*-$TaSe_2$ is shown within the bulk Brillouin zone (hexagonal prism), as calculated with density-functional theory (see Appendix A), with the blue and green surfaces marking two different bands. The change of the dispersion and topology of these two bands with doping is shown in the center for $k_z = 0$ for $\epsilon = \epsilon_0$ (purple contours; also shown within the bulk Brillouin zone), as well as for $\epsilon = \epsilon_{\rm LT} = \epsilon_0 + 0.05\,\text{eV}$ (orange) and $\epsilon > \epsilon_{\rm LT}$ (yellow). The same contours are shown again on top of the gray regular hexagon, representing the projected two-dimensional Brillouin zone, below the dispersion. Also shown are arrows depicting representative $\boldsymbol{q}_{\rm CDW}$ wave vectors for the (3×3) [green], (2×2) [cyan], and $(2\sqrt{3} \times 2\sqrt{3})R30^\circ$ [blue] charge density wave orders. The inset in bottom left shows the top and side views of the 2*H*-$TaSe_2$ lattice structure. Ta and Se atoms are marked with blue and yellow spheres, respectively, and the right rhombic prism indicated with the black solid lines is the unit cell.

II. TOPOLOGY OF ELECTRONIC BANDS OF 2*H* TANTALUM DISELENIDE

2*H*-$TaSe_2$ consists of weakly coupled layers, each of which is made of a plane of tantalum atoms sandwiched between two planes of seleniums. The consecutive layers are rotated by 180° and stacked so that the transition metals are placed on top of each other, as shown in the inset in the bottom left of Fig. 1. The material exhibits a second-order transition into a near-commensurate (3×3) CDW phase at 122 K, followed by a first-order transition which locks the charge order into the (3×3) superlattice at 90 K [35,36]. As suggested by the high critical temperature of the transition into the commensurate CDW, electronic band reconstruction in this phase is quite strong, with the CDW gap 50—100 meV in high-quality crystals [37,38]. For this reason, 2*H*-$TaSe_2$ serves as a model to understand the electronic properties of the isostructural and isoelectronic 2*H*-$NbSe_2$, 2*H*-TaS_2, and 2*H*-NbS_2 in which charge order is weaker so that only the incommensurate phase appears [39,40] (in NbS_2 the CDW order is so fragile that it has only been observed in its two-dimensional limit [41,42]), as well as the mechanisms behind CDW phases in general.

The driving force behind the (3×3) CDW was long debated, partly due to incorrect predictions of the position of the Fermi level [36,43–45]. Experimental and computational studies have established that the Fermi surface, shown in the top left of Fig. 1, consists of **Γ**- and ***K***-centered tube-shaped hole sheets from the first band (blue) and ***M***-centered electron dog-bone sheets from the second (green) and that the CDW is driven by a combination of Fermi-surface nesting and electron-phonon coupling [37,38,46,47]. Because of the quasi-two-dimensional nature of the FS, in what follows we focus on the plane for which the out-of-plane component of the wave vector, k_z, is constant (we choose $k_z = 0$). This allows us to parametrize the two relevant bands as surfaces with energy $\epsilon_i \equiv \epsilon_i(k_x, k_y)$, $(i = 1, 2)$, dependent on the in-plane wave vector $\boldsymbol{k} = (k_x, k_y)$, and shown in the right of Fig. 1 using the same colors, green and blue, as for the bulk FS. The FS then becomes a Fermi contour (FC), indicated in purple solid lines on top of the full FS in the top left as well as on top of the dispersion surfaces ϵ_i and the gray regular hexagon below which represents the two-dimensional Brillouin zone of $TaSe_2$. We denote the Fermi energy of the bulk as $\epsilon = \epsilon_0$.

By inspecting the green dispersion surface, ϵ_2, it can be seen that an increase in the Fermi energy leads to a change of the topology of the Fermi contour. As the energy increases above ϵ_0, the **Γ** pocket decreases slightly. At the same time, the dog-bone pockets grow and connect with each other at energy $\epsilon_{\rm LT} \approx \epsilon_0 + 0.05\,\text{eV}$ and momentum close to $\frac{1}{2}\boldsymbol{K}$, which determines the position of saddle points of the green surface, leading to energy contours as shown in orange in Fig. 1. For energies $\epsilon > \epsilon_{\rm LT}$, the connected dog bones split to form another set of ***K***-centered pockets as well as one more centered around **Γ** (contours shown in yellow). Our work is motivated by the presence of this saddle point, with the potential to tune the Fermi level through a Lifshitz transition—change in the topology of the Fermi contour from the three dog-bone pockets to one **Γ**- and one ***K***-centered pockets—and the question of how it impacts the CDW order.

III. ARPES SPECTRA OF SURFACE-DOPED 2*H*-$TaSe_2$

In order to study the electronic band structure of 2*H*-$TaSe_2$, we use angle-resolved photoemission spectroscopy. Our measurements were taken at the Diamond Light Source (I05) and Advanced Light Source (MERLIN) using photons with energy of 80 eV (see the Supplemental Material (SM) [48] for further details of the ARPES measurements). The map of the Fermi surface as measured at temperature $T = 130\,\text{K}$ is shown in Fig. 2(a), clearly reflecting the single-particle Fermi contour at $\epsilon = \epsilon_0$ shown in purple in Fig. 1. (For direct comparison, in all panels of Fig. 2 we draw in solid red lines the theoretical band cuts obtained using the single-particle tight-binding model discussed in Sec. IV.) When measured at temperature $T = 10\,\text{K}$, Fig. 2(b), the Fermi surface undergoes reconstruction due to the formation of the (3×3) charge density wave [37,38,47,49]: (i) the circular pockets around ***K*** are gapped; instead, a set of six triangular features appears

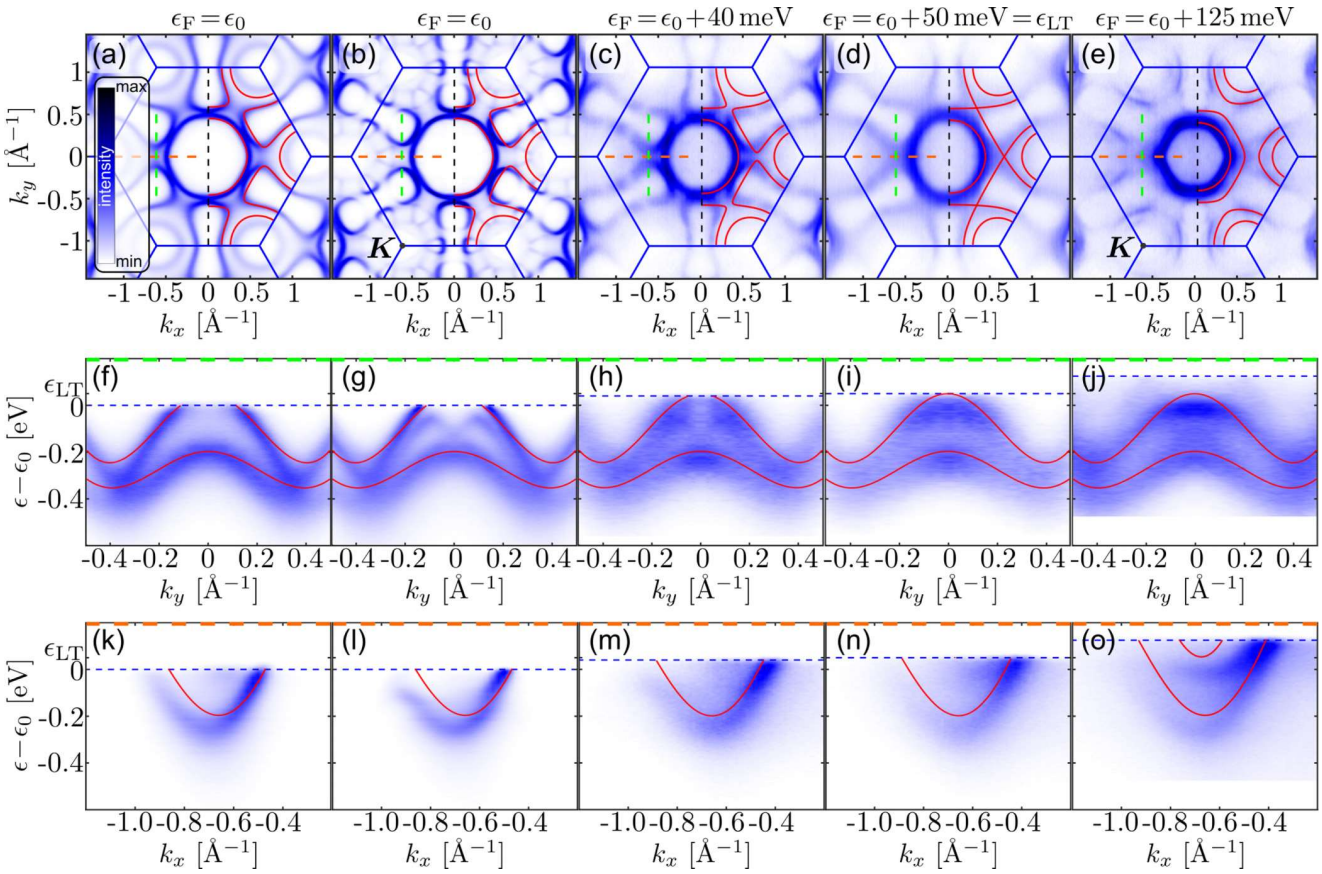

FIG. 2. Angle-resolved photoemission spectra of $2H$-$TaSe_2$: (a), (f), (k) as grown and at temperature $T = 130$ K; (b), (g), (l) at temperature $T = 10$ K and without surface doping; (c), (h), (m) after the first, (d), (i), (n) second, and (e), (j), (o) third dose of surface potassium deposition at $T = 22$ K. The top row [panels (a)–(e)] shows constant-energy maps at the Fermi level; the middle row [panels (f)–(j)] shows spectra along the path crossing the saddle point at $\frac{1}{2}\boldsymbol{K}$ as indicated in green dashed lines in panels (a)–(e); the bottom row [panels (k)–(o)] shows spectra along the path crossing the saddle point, as indicated in orange dashed lines in panels (a)–(e). The blue solid lines indicate the Brillouin zone boundaries, and the red solid lines show bands as predicted by our tight-binding model. The position of the Fermi energy ϵ_F for each case is provided above the constant-energy maps and indicated with the dashed blue line in panels (f)–(o). ARPES spectra were symmetrized with respect to $k_x = 0$ and $k_y = 0$ for better comparisons with calculations (see the SM for a brief discussion of this process [48]); they were all plotted using the same intensity scale with color mapping as shown in the inset of panel (a).

around each Brillouin zone corner; (ii) the dog bones become more rounded and develop gaps along their contour due to Bragg scattering caused by the CDW periodicity; (iii) the $\boldsymbol{\Gamma}$ pocket remains unaffected. Because the CDW superpotential is much weaker than the original periodic lattice potential, the spectral intensity of CDW-folded bands is much weaker than the original, "main" bands. This allows us to track the latter and determine that the connectivity between the dog bones remains unchanged upon CDW formation so that the presence of a Lifshitz transition can still be anticipated if the Fermi energy could be increased.

In order to tune the Fermi energy, we deposit potassium atoms on the surface of our samples at a temperature of 22 K. The small electron affinity of potassium makes it a strong electron donor to most surfaces and leads to n doping of the top layers of the crystal (the low temperature makes intercalation unfeasible). At the same time, surface sensitivity of ARPES means that only the very top layers are probed experimentally [50–52] ($2H$-$TaSe_2$ unit-cell height is $c = 1.228$ nm [53] as compared to the electron escape depth $l \sim 1$ nm [54]). In Figs. 2(c)–2(e), we show the Fermi surfaces as measured after three consecutive potassium depositions (the position of the Fermi energy ϵ_F after each deposition is estimated based on the effective model described in Sec. IV). After the first potassium dose, panel (c), spectral features around the $\boldsymbol{K}$ points disappear, while the most intense signal is from the states around $\boldsymbol{\Gamma}$. Importantly, connectivity between dog bones remains the same as in panels (a) and (b), implying that the Fermi level is still below the dispersion saddle points. Moreover, similar gaps along a dog-bone contour can be identified in panels (b) and (c), indicating persistence of the (3×3) CDW. Following a second potassium dose, panel (d), broadening of the dog bones indicates that the Fermi level is in the close vicinity of the saddle points. While it is difficult to determine whether the change of topology has already occurred at that point, after the third potassium dose and an additional shift of the Fermi level, panel (e), connectivity of the Fermi surface has changed: merging of the dog bones leads to the formation of a circular pocket around $\boldsymbol{K}$, as well as one around $\boldsymbol{\Gamma}$. Note that weak-intensity features connect the

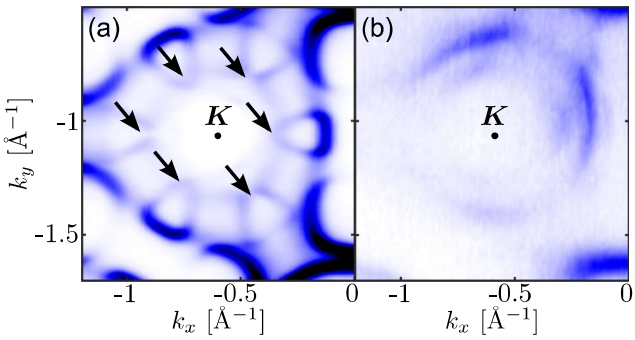

FIG. 3. Closeup on the ARPES Fermi-level maps for 2*H*-$TaSe_2$ in the vicinity of the Brillouin zone corner $\boldsymbol{K}$ [as marked in Figs. 2(b) and 2(e)], (a) before surface doping with potassium and (b) after the third dose of potassium deposition. Black arrows mark the signature of the C_6 symmetry in panel (a). The spectra have been taken at the temperature $T = 10\,\mathrm{K}$ and $T = 22\,\mathrm{K}$ for panels (a) and (b), respectively, below the transition temperature of the commensurate (3×3) charge density wave.

pocket around $\boldsymbol{\Gamma}$ to pockets around $\boldsymbol{K}$—we assign these to the new order we discuss in the rest of the text.

To further confirm that after the third dose of potassium the Fermi level moved above the saddle point, for each of the panels (a)–(e), we show in (f)–(j) the measured band dispersion along the momentum path perpendicular to the $\boldsymbol{\Gamma}$-$\boldsymbol{K}$ direction and passing through the location of the saddle point, as indicated with the green dashed lines. In panels (f)–(h), the higher energy band is not entirely below the Fermi level (note that the weaker intensity, M-shaped band in panel (g) is due to the (3×3) CDW [38]). In contrast, in panels (i) and (j) this band is fully below the Fermi level, which demonstrates that the Lifshitz transition has occurred. The same can be seen in the bottom row of panels (k)–(o), in which we show the measured band dispersion along the $\boldsymbol{K}$-$\boldsymbol{\Gamma}$ direction passing through the saddle point. This is the direction perpendicular to that shown in panels (f)–(j) and along which the dispersion displays opposite curvature. In panels (n) and (o), showing dispersion after the second and third potassium deposition, respectively, one can identify spectral features indicating another band in the vicinity of the Fermi level. This again implies that the Fermi level has crossed the saddle point (we comment further on the ARPES maps and the Lifshitz transition in the SM).

The spectra in all but the first column of Fig. 2 have been taken at a temperature significantly below the transition temperature of the commensurate (3×3) CDW, $T_c \approx 90\,\mathrm{K}$ [35,36]. This allows us to study the interplay between the Lifshitz transition, driven by the single-particle electronic band structure, and the charge density order present in the material. In Fig. 3 we compare the ARPES Fermi-level maps in the vicinity of the Brillouin zone corner $\boldsymbol{K}$ for a pristine 2*H*-$TaSe_2$ surface in the (3×3) state (a), as well as the surface after the final deposition of potassium (b) [zoom-in of parts of the maps in Figs. 2(b) and 2(e), respectively]. Within the single-particle picture, the symmetry of the band dispersion around $\boldsymbol{K}$ is C_3. In panel (a) of Fig. 3, this is reflected in the threefold symmetry of the outer band corresponding to the dark blue intensity contour (interrupted in some places by CDW-induced gaps). The inner band, however, displays a set of six weak-intensity features indicated with black arrows. These features are also due to the (3×3) state, the wave vector of which folds the two otherwise-inequivalent Brillouin zone corners onto each other [38] and hence allows for a weak sixfold rather than exclusively threefold symmetry [37,38]. After the third dose of potassium, panel (b), the C_6 features in the inner band disappear and only the C_3 symmetry remains. Because the Lifshitz transition alone cannot be responsible for this change in symmetry, we conclude that the electronic order has changed as a result of the Fermi-level shift and the (3×3) CDW is no longer present. At the same time, modulation of the photoemission intensity along the outer and inner bands in Fig. 3(b) is indicative of new gaps in the electronic dispersion incompatible with the single-particle picture. We compare the intensity profiles along the inner band before and after potassium doping in the SM.

IV. DISCUSSION

In order to understand the impact of doping and the Lifshitz transition on the charge density order, we describe our system using an effective two-band model based on the tight-binding expansion due to the Ta sites only (as the transition-metal d orbitals provide a predominant contribution to the bands crossing the Fermi level) [37,38,55,56], with one orbital per site. Because of the quasi-two-dimensionality of the bulk band structure, we focus on the dispersion for a constant k_z. For simplicity, we choose $k_z = 0$—the exact choice is, however, not important, as the functional form of the model is independent of k_z, and its parameters are prescribed by experimental data (we comment further on the importance of the out-of-plane dispersion in the SM [48]). The essential features of the band structure can be reproduced by keeping terms up to next-nearest intra- and interlayer neighbors,

$$\hat{\boldsymbol{H}}_{\mathrm{TB}}(\boldsymbol{k}) = f(t_0, t_1, t_2; \boldsymbol{k})\sigma_0 + f(\tilde{t}_0, \tilde{t}_1, \tilde{t}_2; \boldsymbol{k})\sigma_x,$$
$$f(\alpha, \beta, \gamma; \boldsymbol{k}) = \alpha + 2\beta\left[\cos k_x a + 2\cos\frac{k_x a}{2}\cos\frac{\sqrt{3}k_y a}{2}\right] + 2\gamma\left[\cos\sqrt{3}k_y a + 2\cos\frac{3k_x a}{2}\cos\frac{\sqrt{3}k_y a}{2}\right], \tag{1}$$

where σ_0 is a 2×2 identity matrix, σ_x is the x Pauli matrix, $a = 3.43\,\text{Å}$ is the lattice constant of 2*H*-$TaSe_2$, $t_0 = 0.113\,\mathrm{eV}$ is the Ta on-site energy, $\tilde{t}_0 = 0.184\,\mathrm{eV}$ is the direct interlayer coupling, and $t_1 = 0.073\,\mathrm{eV}$ ($\tilde{t}_1 = 0.029\,\mathrm{eV}$) and $t_2 = 0.142\,\mathrm{eV}$ ($\tilde{t}_2 = 0.038\,\mathrm{eV}$) are the nearest and next-nearest intralayer (interlayer) couplings. We fixed our parameters using a hybrid approach in which we fit the model to the ARPES data below the Fermi energy and density-functional-theory calculations above (see Appendix A for the details of the latter). We have also tuned the on-site term t_0 so that $\epsilon_{\mathrm{LT}} = 0$. Our model provides the minimal description which captures the topology of the Fermi contour as a function of the Fermi level and allows us to investigate analytically the saddle points located at $\boldsymbol{k}_{\mathrm{LT}}^{(n)} = \hat{\boldsymbol{R}}_{n\pi/3}[\frac{2\pi}{3a} + \frac{4}{\sqrt{5}a}\delta, 0]^T$,

$n = 0, 1, \ldots, 5$, where $\hat{\boldsymbol{R}}_\theta$ is the operator of rotation by angle θ and $\delta = \frac{t_1+\tilde{t}_1}{6(t_2+\tilde{t}_2)} \ll 1$. While we find that introducing further neighbors or including nonorthogonality corrections allows us to fit the band structure better, the additional parameters complicate the description of the saddle point without providing new insight into the physics.

Following the approach developed in Refs. [57,58] and previously applied, for example, to 2*H*-$NbSe_2$ [59,60], we use the Hamiltonian $\hat{\boldsymbol{H}}_{\mathrm{TB}}(\boldsymbol{k})$ to approximate the electron-phonon matrix element, $g^i_{\boldsymbol{k},\boldsymbol{k}+\boldsymbol{q}}$, which describes scattering of an electron in band i from a state with wave vector $\boldsymbol{k}$ to a state in the same band with wave vector $\boldsymbol{k}+\boldsymbol{q}$ with the simultaneous absorption (emission) of a phonon with wave vector $\boldsymbol{q}$ ($-\boldsymbol{q}$), using gradients of the electronic dispersion,

$$g^i_{\boldsymbol{k},\boldsymbol{k}+\boldsymbol{q}} = [\nabla\epsilon_i(\boldsymbol{k}+\boldsymbol{q}) - \nabla\epsilon_i(\boldsymbol{k})] \cdot \frac{\boldsymbol{q}}{|\boldsymbol{q}|}, \tag{2}$$

where we have ignored a constant prefactor. Moreover, because formation of the charge density wave in 2*H*-$TaSe_2$ involves softening of the longitudinal acoustic phonon [40], we have projected the electron-phonon coupling on the direction of momentum transfer. Also, in the scheme of Refs. [57,58], the symmetric form of the Hamiltonian $\hat{\boldsymbol{H}}_{\mathrm{TB}}$ in Eq. (1) implies that the interband electron-phonon coupling is strictly zero.

The knowledge of the electron-phonon coupling allows us to compute the static generalized susceptibility,

$$D_2(\boldsymbol{q}, \epsilon_{\mathrm{F}}) = \sum_i \int_{BZ} d\boldsymbol{k} \left(g^i_{\boldsymbol{k},\boldsymbol{k}+\boldsymbol{q}}\right)^2 \frac{f[\epsilon_i(\boldsymbol{k})] - f[\epsilon_i(\boldsymbol{k}+\boldsymbol{q})]}{\epsilon_i(\boldsymbol{k}) - \epsilon_i(\boldsymbol{k}+\boldsymbol{q})}, \tag{3}$$

where, for a given Fermi energy ϵ_{F}, $f[\epsilon_i(\boldsymbol{k})]$ is the filling factor of the state with energy $\epsilon_i(\boldsymbol{k})$ in band i and with wave vector $\boldsymbol{k}$, and the integral is over the two-dimensional Brillouin zone. As peaks of $D_2(\boldsymbol{q}, \epsilon_{\mathrm{F}})$ provide information about structural instabilities in the material [57,58,61], we present the plots of $D_2(\boldsymbol{q}, \epsilon_{\mathrm{F}})$ for the high-symmetry directions $\boldsymbol{\Gamma}$-$\boldsymbol{K}$-$\boldsymbol{M}$-$\boldsymbol{\Gamma}$ in Fig. 4(a). The curves for increasing ϵ_{F} have been shifted for clarity, starting from $\epsilon_{\mathrm{F}} = \epsilon_0$ (purple) to $\epsilon_{\mathrm{F}} = \epsilon_0 + 0.25\,\mathrm{eV}$ (red). Two features persist across the whole range of energies: (i) a broad peak in the vicinity of $\frac{2}{3}\boldsymbol{M}$ and (ii) a peak in the vicinity of $\frac{1}{2}\boldsymbol{K}$. The former is related to the (3×3) CDW [46,47]. Given the symmetry of the ARPES constant-energy maps, which excludes considerations of one-dimensional CDW, the latter would imply a $(2\sqrt{3} \times 2\sqrt{3})R30^\circ$ order with a wave vector that nests the saddle points onto each other, as shown with the blue arrow in the bottom right of Fig. 1 (ideal nesting occurs for $\delta \to 0$). Interestingly, another feature, strongly dependent on ϵ_{F}, appears in $D_2(\boldsymbol{q}, \epsilon_{\mathrm{F}})$ at $\boldsymbol{M}$, as highlighted in Fig. 4 by the bright purple dashed oval. This lower peak which develops for ϵ_{F} slightly above ϵ_{LT} [we show in black the curve for $\epsilon_{\mathrm{F}} = \epsilon_{\mathrm{LT}} + 0.075\,\mathrm{eV}$ which corresponds to the Fermi-level estimate for Figs. 2(e) and 2(j)] but disappears for $\epsilon_{\mathrm{F}} \gtrsim \epsilon_{\mathrm{LT}} + 0.15\,\mathrm{eV}$ suggests potential instability towards a (2×2) CDW. Such order would also nest saddle points onto each other as shown with the cyan arrow in Fig. 1 (again, ideal nesting takes place for $\delta \to 0$), albeit in two groups of three.

Motivated by the symmetry breaking shown in Fig. 3, we compare in Fig. 4(b) the Brillouin zones of the uncorrelated phase (black) as well as the (3×3) (blue), $(2\sqrt{3} \times 2\sqrt{3})R30^\circ$ (green), and (2×2) (red) CDW. Note that for both the (3×3) and $(2\sqrt{3} \times 2\sqrt{3})R30^\circ$ superlattices, the two originally inequivalent zone corners $\boldsymbol{K}$ and $\boldsymbol{K}'$ are folded onto $\boldsymbol{\Gamma}$. In contrast, they remain inequivalent for the (2×2) superlattice, guaranteeing C_3 symmetry of dispersions in their vicinity in agreement with Fig. 3(b). In Fig. 4(c) we show the spectral function in the vicinity of the corner $\boldsymbol{K}$, computed at the energy $\epsilon_0 + 0.125\,\mathrm{eV}$ for the (2×2) CDW using the approach described in Appendix B. In agreement with Fig. 3(b), each band is divided into three arcs, with the spectral weight decreasing where the contours cross the red lines, which indicate the boundaries of the (2×2) Brillouin zone. This suggests that gaps observed in Fig. 3(b) can be understood as a consequence of Bragg scattering of electrons by the newly formed (2×2) superlattice. We show in the SM [48] that similar

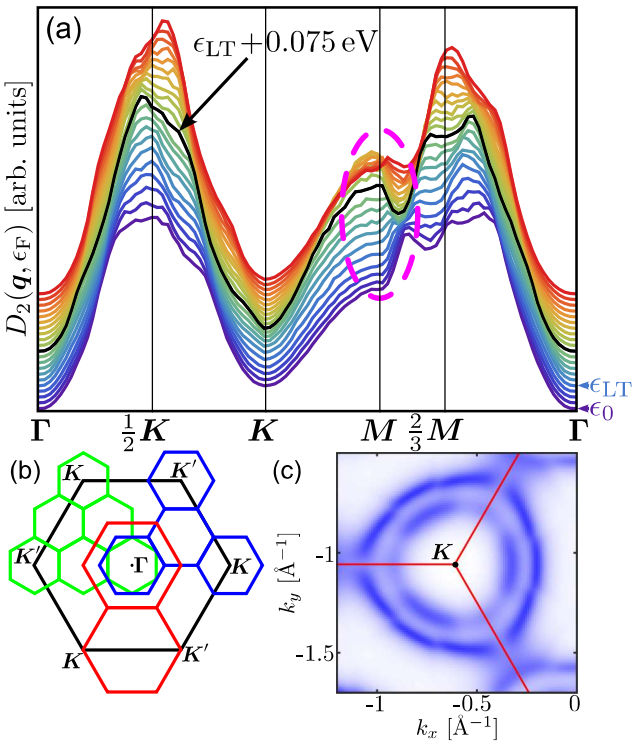

FIG. 4. (a) Generalized static susceptibility $D_2(\boldsymbol{q}, \epsilon_{\mathrm{F}})$ as a function of the Fermi level ϵ_{F} from $\epsilon_{\mathrm{F}} = \epsilon_0$ (purple) to $\epsilon_{\mathrm{F}} = \epsilon_0 + 0.25\,\mathrm{eV}$ (red) in steps of 0.0125 eV, along the high-symmetry Brillouin zone directions. The curves have been shifted vertically for clarity. On the right we indicate the curves corresponding to the Fermi energy of the pristine material, $\epsilon_{\mathrm{F}} = \epsilon_0$, as well as for the Fermi energy at the saddle point, $\epsilon_{\mathrm{F}} = \epsilon_{\mathrm{LT}}$. The curve for $\epsilon_{\mathrm{F}} = \epsilon_0 + 0.125\,\mathrm{eV} = \epsilon_{\mathrm{LT}} + 0.075\,\mathrm{eV}$, corresponding to the Fermi-level estimate for Figs. 2(e) and 2(j), is shown in black. The bright purple dashed oval highlights a susceptibility feature at $\boldsymbol{M}$ which appears in the energy range $\sim$0.1 eV above ϵ_{LT}. (b) Comparison of Brillouin zones of the uncorrelated phase (black) and the (3×3) (blue), $(2\sqrt{3} \times 2\sqrt{3})R30^\circ$ (green), and (2×2) (red) superlattices. (c) Spectral function in the vicinity of $\boldsymbol{K}$ computed at the energy $\epsilon_0 + 0.125\,\mathrm{eV}$ for the (2×2) CDW using the model described in Appendix B with broadening $\eta = 0.1\,\mathrm{eV}$. The red lines depict the boundaries of the (2×2) superlattice Brillouin zone.

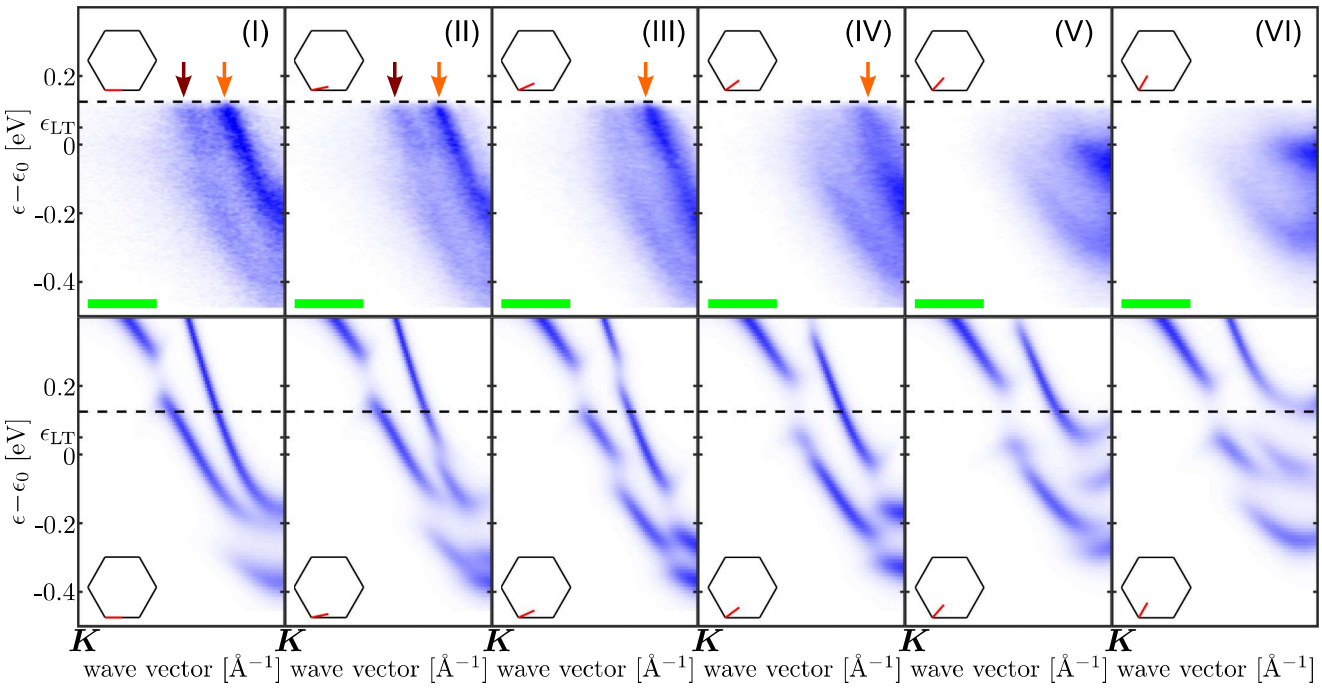

FIG. 5. Comparison of experimental (top) and simulated (bottom) ARPES intensities following the final potassium deposition for wave-vector cuts at different angles starting from the $\boldsymbol{K}$ point of the Brillouin zone (as indicated with the red lines in the insets of each panel). The Fermi energy, $\epsilon_F = \epsilon_0 + 0.125\,\text{eV}$, is indicated with the dashed black line. In the top row, the dark red and orange arrows indicate the momentum at which the inner and outer band, respectively, cross the Fermi level. All cuts cover the same distance in k space; the green scale bars in the top row correspond to 0.2 Å^{-1}. For the theoretical plots we used energy broadening $\eta = 0.05\,\text{eV}$.

spectral function maps for the (3×3) and $(2\sqrt{3} \times 2\sqrt{3})R30^\circ$ phases display features which disagree with our observations.

While both the $(2\sqrt{3} \times 2\sqrt{3})R30^\circ$ and (2×2) phases lead to nesting of the saddle points with each other, further support for the latter comes from studying a minimal model describing such coupling which we present in Appendix C. For the (2×2) phase, introducing attractive coupling between electrons in the vicinity of the saddle points leads to opening of a gap at a filling corresponding to the position of the Fermi level at the saddle point for the uncorrelated state. This agrees with experimental observations—gap above the saddle point in Fig. 2(j). At the same time, no such gap opens in the $(2\sqrt{3} \times 2\sqrt{3})R30^\circ$ phase. We have also confirmed that formation of a (2×2) phase, as described by our effective model, lowers the total electron energy of the system as compared to the uncorrelated state (see further discussion in the SM [48]). This energetic benefit is due to the new phase opening gaps in the electronic spectrum which remove the van Hove singularities located at the saddle points from the vicinity of the Fermi level.

In Fig. 5 we show in the top row the measured ARPES intensities for the sample after the third deposition of potassium for k-space cuts in different directions from $\boldsymbol{K}$, from $\boldsymbol{K}$ towards $\boldsymbol{M}$ (first panel) to $\boldsymbol{K}$ towards $\boldsymbol{\Gamma}$ (last panel), in constant intervals. These cuts provide further information on the evolution of the band gaps observed as discontinuities of the Fermi contour in Fig. 3(b). We mark with maroon and orange arrows the wave vectors at which the two bands, which correspond to the inner and outer contours, respectively, around $\boldsymbol{K}$ in Fig. 3(b), cross the Fermi level, $\epsilon_F = \epsilon_0 + 0.125\,\text{eV}$ (the latter is indicated in all the panels by the black dashed line). In panel (III) the intensity of the inner band gradually fades away and the band exhibits a gaplike feature at the Fermi level. This feature persists in the remaining panels, (IV)–(VI). In turn, the outer band becomes flatter as the angle increases, suggestive of the formation of a gap in panels (V) and (VI) (the latter is equivalent to the $\boldsymbol{K}$-$\boldsymbol{\Gamma}$ direction).

In the theoretical plots in the bottom row of Fig. 5, we have deliberately shown the intensity for the states above the Fermi level to illustrate the evolution of the gaps in the outer and inner bands for different k-space cuts. Crucially, the trend of a gap at the Fermi level appearing first in the inner band, followed by a gap in the outer band, is preserved. In the inner band this is due to a band gap moving down in energy as the direction of the cut moves from $\boldsymbol{K}$-$\boldsymbol{M}$ to $\boldsymbol{K}$-$\boldsymbol{\Gamma}$. In the outer band the gap appears due to the coupling of the saddle points with each other and is hence maximized along the $\boldsymbol{K}$-$\boldsymbol{\Gamma}$ direction which passes through a saddle point. With the help of an effective model of coupled saddle points (see Appendix C), this maximum gap can be estimated as $\sim 3\Delta$, with Δ the intraband CDW gap parameter. While the data presented here were obtained using photons with linear horizontal polarization, we have performed measurements using linear vertical polarization as well (we present a comparison of the two in the SM [48]). The agreement between the two polarizations and the theoretically calculated spectral function suggests that effects related to the polarization of the incoming light or matrix element effect [62,63] do not play any role in our observations. Also, we do not observe any novel bandlike features in our spectra, which are expected if the modifications of the dispersion are due to ordering of potassium on the surface

of $TaSe_2$ (see [48] for an additional discussion of potassium deposition).

As the bulk of our crystal necessarily continues to host the (3×3) charge density wave, it might be interesting to explore the crossover between the bulk and the surface-correlated states, possibly using soft-x-ray ARPES with a longer photoelectron attenuation depth than traditional photoemission [64]. At the same time, because the change of charge-density order relies on nesting of electronic van Hove singularities, the (2×2) phase should be further stabilized in thin enough (with a number of layers $\sim$2) doped or gated crystals of $TaSe_2$, similarly to the case of TaS_2 [65]. Thin flakes also have the advantage that the Fermi level could be shifted using electrostatic gating rather than by surface deposition of alkali atoms, as done here. In that case, scanning transmission microscopy could be used to observe the existence of the new CDW directly in real space (in contrast to our situation in which, as we discuss in the SM, the deposited potassium prevents access to the $TaSe_2$ surface). Another approach would be alloying of Ta with another metal. For example, tungsten atoms have one more d electron than tantalum, so that in $Ta_{1-x}W_xSe_2$ the Fermi level crosses the vHS for a small W concentration, x [66]. Moreover, in $2H$-$NbSe_2$, the Fermi level lies above a saddle-point equivalent to the one discussed here, and the material displays the incommensurate (3×3) order [46]. (This matches up with the persistence of the peak corresponding to the (3×3) instability in generalized susceptibility as a function of the Fermi level in Fig. 4(a).) This means that in $Ta_{1-x}Nb_xSe_2$, the Fermi level has to cross the saddle point for some Nb concentration x (as Nb is isoelectronic with Ta, this is because of a deformation of the band structure which should occur smoothly between the two pure compositions, rather than due to electronic doping per se). In both cases, engineering of the band structure might allow study of the presence of the (2×2) state without obstructing the surface.

The presence of saddle points roughly midway between $\boldsymbol{\Gamma}$ and $\boldsymbol{K}$ in the d-orbital-derived bands is a generic feature of the band structure of all $2H$ transition-metal dichalcogenides (including the semiconducting members of the family), and so we suggest that several seemingly unrelated observations of a (2×2) superlattice in these materials are connected by the underlying mechanism of van Hove singularity nesting. In the metallic $TaSe_2$, TaS_2, $NbSe_2$, and NbS_2, as discussed here, the relevant bands contribute to the Fermi surface and so the saddle points are relatively close to the Fermi level. Some spectroscopy measurements suggest a weak (2×2) charge density wave can coexist with the (3×3) order in $NbSe_2$ [67]. In the same work, no (2×2) superlattice was observed in $TaSe_2$ and TaS_2. However, this CDW order was observed in chalcogen-poor $TaSe_2$ [36], which is consistent with the driving mechanism as discussed here, given that chalcogen vacancies effectively n-dope the material [68–70]. A (2×2) superlattice was also observed in intercalated $TaSe_2$ (and so was highly n-doped), although the origin was suggested to be due to intercalant ordering rather than a new charge-density order [71]. In semiconductors like MoS_2 or WSe_2, the saddle points can be found in the lowest-lying conduction band. Moving the Fermi level into their vicinity requires a considerable doping, achievable, for example, by intercalation, as suggested by the observations on MoS_2 [72].

V. SUMMARY

To summarize, by depositing potassium on bulk $2H$-$TaSe_2$, we have induced band bending near the surface of the crystal which allowed us to tune the Fermi level past a saddle point of the quasi-two-dimensional dispersion. We have used ARPES to observe the interplay between the resulting single-particle Lifshitz transition and the (3×3) CDW existing in the material. With the help of an effective two-band model fitted using both the ARPES data and density-functional theory, we found that the resulting change in the Fermi surface is consistent with a change in CDW geometry from (3×3) to (2×2). For the latter phase, spectral reconstruction nests saddle-point van Hove singularities close to the Fermi level.

The saddle-point nesting mechanism of CDW formation was proposed in 1975 [20], shortly after the first experimental observations of CDWs in dimensions higher than one. Whereas in one-dimensional metals the weak-coupling nesting (Peierls) mechanism generically leads to CDW formation, in two and three dimensions a single wave vector will typically not connect large regions of the Fermi surface, and it was originally unclear how CDWs could be energetically beneficial. While saddle-point nesting addressed this issue by taking advantage of the high density of states at the van Hove singularities, it is now accepted that in most transition-metal dichalcogenides, CDWs are not generated by weak-coupling nesting instabilities, instead relying on the detailed structure of the interactions [59,73]. Our measurements on potassium-doped $2H$-$TaSe_2$ could be the first observation of changes in the electronic dispersion due to the formation of saddle-point-induced CDW order in transition-metal dichalcogenides, as originally proposed.

Given the differences in mechanisms driving the (3×3) and (2×2) CDW phases, it would be interesting to investigate how different their interplay with superconductivity is. For example, recently, a pair density wave (PDW) was observed in $2H$-$NbSe_2$ using scanning Josephson tunneling microscopy [74]. In a PDW it is Cooper pairs rather than electrons which break the symmetry of the crystal structure. This was the first evidence of a PDW outside the cuprate high-temperature superconductors and, owing to the remarkable similarity of the band structures of transition-metal dichalcogenides, it would seem highly likely that a PDW could also be observed in $2H$-$TaSe_2$ (albeit requiring temperatures below the critical temperature, 0.13 K, for the pristine material [75], in contrast to 7 K for $NbSe_2$ [76]). In such a case, we might expect a similar change in PDW geometry under doping, as discussed here for the CDW.

Finally, a doping-controlled change in CDW geometry from (3×3) to (2×2) would constitute a quantum phase transition, indicating a presence of an underlying quantum critical point. A doping-based quantum phase transition is suspected to lead to the superconducting dome in the hole-doped cuprates [77,78], and the opportunity to study a similar scenario in the absence of high-temperature superconductivity could help disentangle the complicated knot of intertwined phenomena accompanying that state. In the case of potassium-doped $2H$-$TaSe_2$, the quantum phase transition would occur in the vicinity of a Lifshitz transition. The resulting high density of states makes the system highly tunable, leading to a change

in the electron, crystal, and phonon structures. Access to such a controllable quantum phase transition would make doped 2*H*-$TaSe_2$ a promising candidate for future studies as a source of new exotic phenomena.

ACKNOWLEDGMENTS

We thank E. Da Como and D. Wolverson for their comments on the manuscript. This work has been supported by the UK Engineering and Physical Sciences Research Council (EPSRC) through the Centre for Doctoral Training in Condensed Matter Physics (CDT-CMP), Grant No. EP/L015544/1. Y.L. acknowledges support from the National Natural Science Foundation of China (Grant No. 12104304) and the Fundamental Research Funds for the Central Universities (2042023kf0107). J.J. acknowledges support from the National Natural Science Foundation of China (Grant No. 12174362). We also acknowledge beam time allocations at the MERLIN beamline of the Advanced Light Source, U.S.A., and the I05 beamline of the Diamond Light Source, U.K., and support from beamline scientists J. Denlinger, T. Kim, and M. Hoesch.

APPENDIX A: *AB INITIO* CALCULATION OF BAND STRUCTURE

In order to obtain the bulk band structure of 2*H*-$TaSe_2$ shown in the top left of Fig. 1, we used the QUANTUM EXPRESSO package [79], with relativistic pseudopotentials constructed using the PSLibrary [80] for the local-density approximation and a $10 \times 10 \times 10$ Monkhorst-Pack grid [81] for the bulk crystal. From this we extracted the data for $k_z = 0$ plane (we show in the Supplemental Material [48] that the dependence of the dispersion on k_z is negligible), which we used together with the experimental data to fit our tight-binding model. Note that density-functional-theory calculations anticipate an incorrect position of the Fermi level. This is a well-known effect in these materials [47], which was corrected by comparison to the experiment.

APPENDIX B: MODELING ARPES INTENSITY OF THE (2 × 2) CDW

We can simulate theoretically the experimental ARPES intensities by implementing Bragg scattering on a (2×2) superlattice,

$$\hat{\boldsymbol{H}}_{(2\times2)} = \begin{bmatrix} \hat{\boldsymbol{H}}(\boldsymbol{k}) & \hat{\boldsymbol{\Delta}} & \hat{\boldsymbol{\Delta}} & \hat{\boldsymbol{\Delta}} \\ \hat{\boldsymbol{\Delta}} & \hat{\boldsymbol{H}}(\boldsymbol{k}+\boldsymbol{G}_0) & \hat{\boldsymbol{\Delta}} & \hat{\boldsymbol{\Delta}} \\ \hat{\boldsymbol{\Delta}} & \hat{\boldsymbol{\Delta}} & \hat{\boldsymbol{H}}(\boldsymbol{k}+\boldsymbol{G}_1) & \hat{\boldsymbol{\Delta}} \\ \hat{\boldsymbol{\Delta}} & \hat{\boldsymbol{\Delta}} & \hat{\boldsymbol{\Delta}} & \hat{\boldsymbol{H}}(\boldsymbol{k}+\boldsymbol{G}_2) \end{bmatrix}, \tag{B1}$$

where $\hat{\boldsymbol{H}}(\boldsymbol{k}) = \frac{1}{2}(\sigma_x + \sigma_z)\hat{\boldsymbol{H}}_{\mathrm{TB}}(\sigma_x + \sigma_z)$ is the diagonal form of the tight-binding Hamiltonian $\hat{\boldsymbol{H}}_{\mathrm{TB}}$ from Eq. (1), σ_z is the z Pauli matrix, $\boldsymbol{G}_j = \hat{\boldsymbol{R}}_{2j\pi/3}[0, \frac{2\pi}{\sqrt{3}a}]$, and $\hat{\boldsymbol{\Delta}}$ describes the CDW gap. For simplicity we take $\hat{\boldsymbol{\Delta}}$ as constant and diagonal (no coupling between bands of different character). Guided by the effective description, Eq. (C2) in Appendix C, we require

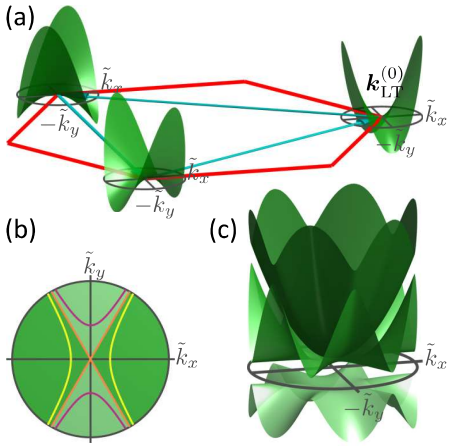

FIG. 6. (a) Schematic of the minimal model for the coupling between the saddle points in the (2×2) charge density wave phase. The red hexagon represents the Brillouin zone of the (2×2) superlattice, and the green surfaces show the electronic dispersion in the vicinity of three saddle points coupled by the superlattice reciprocal vectors indicated with the cyan arrows. (b) Constant-energy contours in the vicinity of a saddle point as described by $\hat{\boldsymbol{H}}_{\mathrm{LT}}(\tilde{\boldsymbol{k}})$ in Eq. (C1) for the energies $\epsilon < \epsilon_{\mathrm{LT}}$ (yellow), $\epsilon = \epsilon_{\mathrm{LT}}$ (orange), and $\epsilon > \epsilon_{\mathrm{LT}}$ (purple). For $\epsilon = \epsilon_{\mathrm{LT}}$, one-third of the electronic states are occupied as illustrated in light green. (c) The electronic dispersion in the vicinity of a saddle point reconstructed by attractive (2×2)-periodic coupling.

$\hat{\boldsymbol{\Delta}}_{11} < 0$, and we find that we can obtain qualitative agreement with experiment by using a single parameter if $\hat{\boldsymbol{\Delta}} = \tilde{\Delta}\sigma_z$, $\tilde{\Delta} < 0$. In the theoretical plots in Figs. 4 and 5, we have used $\tilde{\Delta} = -60\,\mathrm{meV}$ and simulated the ARPES intensity using the wave-vector-resolved spectral function,

$$A(\boldsymbol{k}) = -\frac{1}{\pi}\sum_n \Im[\langle \boldsymbol{k}, n|(\hat{\boldsymbol{H}}_{(2\times2)} - \epsilon - i\eta))^{-1}|\boldsymbol{k}, n\rangle], \tag{B2}$$

where $\Im[x]$ stands for the imaginary part of x, $|\boldsymbol{k}, n\rangle$ denotes the state with wave vector $\boldsymbol{k}$ in the band n, and η is the phenomenological energy broadening. In Fig. 4(c) we have used $\eta = 0.1\,\mathrm{eV}$, and in the bottom row of Fig. 5, $\eta = 0.05\,\mathrm{eV}$.

APPENDIX C: EFFECTIVE MODEL OF SADDLE-POINT COUPLING

Because of the energy separation between the bands, we only focus here on the band $\epsilon_2(\boldsymbol{k})$ that contains the saddle point of interest. For $\delta = 0$ the dispersion in the vicinity of the saddle point at $\boldsymbol{k}_{\mathrm{LT}}^{(0)}$, shown in the right of Fig. 6(a), can be described by the effective Hamiltonian,

$$\hat{\boldsymbol{h}}(\tilde{\boldsymbol{k}}) = \frac{3a^2(t_2 + \tilde{t}_2)}{2}\left(3\tilde{k}_x^2 - \tilde{k}_y^2\right), \tag{C1}$$

where $\tilde{\boldsymbol{k}} = (\tilde{k}_x, \tilde{k}_y) = \boldsymbol{k} - \boldsymbol{k}_{\mathrm{LT}}^{(0)}$ is the wave vector measured from the saddle point (we discuss corrections to this minimal model arising from $\delta \neq 0$ in [48]). As shown in light green in Fig. 6(b), for the Fermi level positioned exactly at such a saddle point, a third of the electronic states are occupied while two-thirds remain empty. The (2×2) CDW-induced superlattice provides a new source of Bragg scattering which couples

the saddle point at $\boldsymbol{k}_{\mathrm{LT}}^{(0)}$ to two other saddle points at $\boldsymbol{k}_{\mathrm{LT}}^{(2)}$ and $\boldsymbol{k}_{\mathrm{LT}}^{(4)}$. We present this coupling schematically in Fig. 6(a), with the red hexagon indicating the Brillouin zone of the (2×2) superlattice and the cyan arrows its basic reciprocal vectors which connect the saddle points. A simple description of this coupling is provided by the Hamiltonian,

$$\hat{\boldsymbol{h}}_{(2\times2)} = \begin{bmatrix} \hat{\boldsymbol{h}}(\tilde{\boldsymbol{k}}) & \Delta & \Delta \\ \Delta & \hat{\boldsymbol{h}}\big(\hat{\boldsymbol{R}}_{\frac{2\pi}{3}}\tilde{\boldsymbol{k}}\big) & \Delta \\ \Delta & \Delta & \hat{\boldsymbol{h}}\big(\hat{\boldsymbol{R}}_{\frac{4\pi}{3}}\tilde{\boldsymbol{k}}\big) \end{bmatrix}, \tag{C2}$$

where the diagonal terms describe each of the three saddle points and Δ is the coupling due to the CDW order, which we take to be real and a constant across the small area of the Brillouin zone that is of relevance. The Hamiltonian coupling saddle points at $\boldsymbol{k}_{\mathrm{LT}}^{(1)}$, $\boldsymbol{k}_{\mathrm{LT}}^{(3)}$, and $\boldsymbol{k}_{\mathrm{LT}}^{(5)}$ can be obtained by setting $\tilde{\boldsymbol{k}} \to -\tilde{\boldsymbol{k}}$ in $\hat{\boldsymbol{H}}_{(2\times2)}$.

Diagonalizing $\hat{\boldsymbol{h}}_{(2\times2)}$ exactly at the saddle point, $\tilde{\boldsymbol{k}} = 0$, gives energies $\epsilon = 2\Delta$ and $\epsilon = -\Delta$, with the latter doubly degenerate. For attractive interaction, $\Delta < 0$, such a spectrum results in a gap at one-third filling. The full spectrum of the Hamiltonian $\hat{\boldsymbol{h}}_{(2\times2)}$ for $\Delta < 0$ is presented in Fig. 6(c). Note that a gap separates the lowest band, shown in light green, from the higher ones, in agreement with experiment where no ARPES intensity is seen above the saddle point, Fig. 2(j). As we demonstrate in the SM [48], a gap does not appear at one-third filling in the case of the $(2\sqrt{3} \times 2\sqrt{3})R30^\circ$ order.

[1] M. I. Kaganov and I. M. Lifshits, Electron theory of metals and geometry, Sov. Phys. Usp. **22**, 904 (1979).

[2] C. W. Chu, T. F. Smith, and W. E. Gardner, Study of Fermi-surface topology changes in rhenium and dilute Re solid solutions from T_c measurements at high pressure, Phys. Rev. B **1**, 214 (1970).

[3] B. K. Godwal, A. Jayaraman, S. Meenakshi, R. S. Rao, S. K. Sikka, and V. Vijayakumar, Electronic topological and structural transition in $AuIn_2$ under pressure, Phys. Rev. B **57**, 773 (1998).

[4] T. Nishimura, H. Sakai, H. Mori, K. Akiba, H. Usui, M. Ochi, K. Kuroki, A. Miyake, M. Tokunaga, Y. Uwatoko, K. Katayama, H. Murakawa, and N. Hanasaki, Large enhancement of thermoelectric efficiency due to a pressure-induced Lifshitz transition in SnSe, Phys. Rev. Lett. **122**, 226601 (2019).

[5] Y. Wu, N. H. Jo, M. Ochi, L. Huang, D. Mou, S. L. Bud'ko, P. C. Canfield, N. Trivedi, R. Arita, and A. Kaminski, Temperature-induced Lifshitz transition in WTe_2, Phys. Rev. Lett. **115**, 166602 (2015).

[6] Y. Zhang, C. Wang, L. Yu, G. Liu, A. Liang, J. Huang, S. Nie, X. Sun, Y. Zhang, B. Shen, J. Liu, H. Weng, L. Zhao, G. Chen, X. Jia, C. Hu, Y. Ding, W. Zhao, Q. Gao, C. Li *et al.*, Electronic evidence of temperature-induced Lifshitz transition and topological nature in $ZrTe_5$, Nat. Commun. **8**, 15512 (2017).

[7] F. C. Chen, Y. Fei, S. J. Li, Q. Wang, X. Luo, J. Yan, W. J. Lu, P. Tong, W. H. Song, X. B. Zhu, L. Zhang, H. B. Zhou, F. W. Zheng, P. Zhang, A. L. Lichtenstein, M. I. Katsnelson, Y. Yin, N. Hao, and Y. P. Sun, Temperature-induced Lifshitz transition and possible excitonic instability in ZrSiSe, Phys. Rev. Lett. **124**, 236601 (2020).

[8] N. Kozlova, J. Hagel, M. Doerr, J. Wosnitza, D. Eckert, K.-H. Muller, L. Schultz, I. Opahle, S. Elgazzar, M. Richter, G. Goll, H. v. Lohneysen, G. Zwicknagl, T. Yoshino, and T. Takabatake, Magnetic-field-induced band-structure change in CeBiPt, Phys. Rev. Lett. **95**, 086403 (2005).

[9] P. M. C. Rourke, A. McCollam, G. Lapertot, G. Knebel, J. Flouquet, and S. R. Julian, Magnetic-field dependence of the $YbRh_2Si_2$ Fermi surface, Phys. Rev. Lett. **101**, 237205 (2008).

[10] M. Orlita, P. Neugebauer, C. Faugeras, A.-L. Barra, M. Potemski, F. M. D. Pellegrino, and D. M. Basko, Cyclotron motion in the vicinity of a Lifshitz transition in graphite, Phys. Rev. Lett. **108**, 017602 (2012).

[11] Y. Okamoto, A. Nishio, and Z. Hiroi, Discontinuous Lifshitz transition achieved by band-filling control in Na_xCoO_2, Phys. Rev. B **81**, 121102(R) (2010).

[12] M. R. Norman, J. Lin, and A. J. Millis, Lifshitz transition in underdoped cuprates, Phys. Rev. B **81**, 180513(R) (2010).

[13] D. LeBoeuf, N. Doiron-Leyraud, B. Vignolle, M. Sutherland, B. J. Ramshaw, J. Levallois, R. Daou, F. Laliberte, O. Cyr-Choiniere, J. Chang, Y. J. Jo, L. Balicas, R. Liang, D. A. Bonn, W. N. Hardy, C. Proust, and L. Taillefer, Lifshitz critical point in the cuprate superconductor $YBa_2Cu_3O_y$ from high-field Hall effect measurements, Phys. Rev. B **83**, 054506 (2011).

[14] I. M. Lifshitz, Anomalies of electron characteristics of a metal in the high pressure region, Sov. Phys. JETP **11**, 1130 (1960).

[15] Ya. M. Blanter, M. I. Kaganov, A. V. Pantsulaya, and A. A. Varlamov, The theory of electronic topological transitions, Phys. Rep. **245**, 159 (1994).

[16] L. van Hove, The occurrence of singularities in the elastic frequency distribution of a crystal, Phys. Rev. **89**, 1189 (1953).

[17] Ya. M. Blanter, V. Tognetti, and A. A. Varlamov, On the manifestation of symmetry and dimensionality for electronic systems in Lifshitz topological transitions, Phys. Lett. A **193**, 325 (1994).

[18] R. S. Markiewicz, A survey of the Van Hove scenario for high-t_c superconductivity with special emphasis on pseudogaps and striped phases, J. Phys. Chem. Solids **58**, 1179 (1997).

[19] D. Yudin, D. Hirschmeier, H. Hafermann, O. Eriksson, A. I. Lichtenstein, and M. I. Katsnelson, Fermi condensation near van Hove singularities within the Hubbard model on the triangular lattice, Phys. Rev. Lett. **112**, 070403 (2014).

[20] T. M. Rice and G. K. Scott, New mechanism for a charge-density-wave instability, Phys. Rev. Lett. **35**, 120 (1975).

[21] K. Kim, S. Kim, J. S. Kim, H. Kim, J.-H. Park, and B. I. Min, Importance of the van Hove singularity in superconducting $PdTe_2$, Phys. Rev. B **97**, 165102 (2018).

[22] R. Hlubina, S. Sorella, and F. Guinea, Ferromagnetism in the two dimensional $t - t'$ Hubbard model at the Van Hove density, Phys. Rev. Lett. **78**, 1343 (1997).

[23] S. Benhabib, A. Sacuto, M. Civelli, I. Paul, M. Cazayous, Y. Gallais, M.-A. Measson, R. D. Zhong, J. Schneeloch, G. D. Gu, D. Colson, and A. Forget, Collapse of the normal-state pseudogap at a Lifshitz transition in the $Bi_2Sr_2CaCu_2O_{8+\delta}$ cuprate superconductor, Phys. Rev. Lett. **114**, 147001 (2015).

[24] H. Bragança, S. Sakai, M. C. O. Aguiar, and M. Civelli, Correlation-driven Lifshitz transition at the emergence of the pseudogap phase in the two-dimensional Hubbard model, Phys. Rev. Lett. **120**, 067002 (2018).

[25] X. Wu, T. Schwemmer, T. Muller, A. Consiglio, G. Sangiovanni, D. Di Sante, Y. Iqbal, W. Hanke, A. P. Schnyder, M. M. Denner, M. H. Fischer, T. Neupert, and R. Thomale, Nature of unconventional pairing in the kagome superconductors AV_3Sb_5 (A = K, Rb, Cs), Phys. Rev. Lett. **127**, 177001 (2021).

[26] Y.-X. Jiang, J.-X. Yin, M. M. Denner, N. Shumiya, B. R. Ortiz, G. Xu, Z. Guguchia, J. He, M. S. Hossain, X. Liu, J. Ruff, L. Kautzsch, S. S. Zhang, G. Chang, I. Belopolski, Q. Zhang, T. A. Cochran, D. Multer, M. Litskevich, Z.-J. Cheng *et al.*, Unconventional chiral charge order in kagome superconductor KV_3Sb_5, Nat. Mater. **20**, 1353 (2021).

[27] Y. Hu, X. Wu, B. R. Ortiz, S. Ju, X. Han, J. Ma, N. C. Plumb, M. Radovic, R. Thomale, S. D. Wilson, A. P. Schnyder, and M. Shi, Rich nature of Van Hove singularities in kagome superconductor CsV_3Sb_5, Nat. Commun. **13**, 2220 (2022).

[28] M. Kang, S. Fang, J.-K. Kim, B. R. Ortiz, S. H. Ryu, J. Kim, J. Yoo, G. Sangiovanni, D. Di Sante, B.-G. Park, C. Jozwiak, A. Bostwick, E. Rotenberg, E. Kaxiras, S. D. Wilson, J.-H. Park, and R. Comin, Twofold van Hove singularity and origin of charge order in topological kagome superconductor CsV_3Sb_5, Nat. Phys. **18**, 301 (2022).

[29] Y. Cao, V. Fatemi, S. Fang, K. Watanabe, T. Taniguchi, E. Kaxiras, and P. Jarillo-Herrero, Unconventional superconductivity in magic-angle graphene superlattices, Nature (London) **556**, 43 (2018).

[30] R. Nandkishore, L. S. Levitov, and A. V. Chubukov, Chiral superconductivity from repulsive interactions in doped graphene, Nat. Phys. **8**, 158 (2012).

[31] P. Rosenzweig, H. Karakachian, D. Marchenko, K. Kuster, and U. Starke, Overdoping graphene beyond the van Hove singularity, Phys. Rev. Lett. **125**, 176403 (2020).

[32] A. Varlet, D. Bischoff, P. Simonet, K. Watanabe, T. Taniguchi, T. Ihn, K. Ensslin, M. Mucha-Kruczynski, and V. I. Fal'ko, Anomalous sequence of quantum Hall liquids revealing a tunable Lifshitz transition in bilayer graphene, Phys. Rev. Lett. **113**, 116602 (2014).

[33] A. Varlet, M. Mucha-Kruczynski, D. Bischoff, P. Simonet, T. Taniguchi, K. Watanabe, V. Fal'ko, T. Ihn, and K. Ensslin, Tunable Fermi surface topology and Lifshitz transition in bilayer graphene, Synth. Met. **210**, 19 (2015).

[34] H. Zhou, T. Xie, T. Taniguchi, K. Watanabe, and A. F. Young, Superconductivity in rhombohedral trilayer graphene, Nature (London) **598**, 434 (2021).

[35] K. Rossnagel, On the origin of charge-density waves in select layered transition-metal dichalcogenides, J. Phys.: Condens. Matter **23**, 213001 (2011).

[36] J. A. Wilson, F. J. Di Salvo, and S. Mahajan, Charge-density waves and superlattices in the metallic layered transition metal dichalcogenides, Adv. Phys. **24**, 117 (1975).

[37] K. Rossnagel, E. Rotenberg, H. Koh, N. V. Smith, and L. Kipp, Fermi surface, charge-density-wave gap, and kinks in 2H-$TaSe_2$, Phys. Rev. B **72**, 121103(R) (2005).

[38] Y. W. Li, J. Jiang, H. F. Yang, D. Prabhakaran, Z. K. Liu, L. X. Yang, and Y. L. Chen, Folded superstructure and degeneracy-enhanced band gap in the weak-coupling charge density wave system 2H-$TaSe_2$, Phys. Rev. B **97**, 115118 (2018).

[39] M. Naito and S. Tanaka, Electrical transport properties in 2H-NbS_2, -$NbSe_2$, -TaS_2, and -$TaSe_2$, J. Phys. Soc. Jpn. **51**, 219 (1982).

[40] D. E. Moncton, J. D. Axe, and F. J. DiSalvo, Neutron scattering study of the charge-density wave transitions in 2H-$TaSe_2$ and 2H-$NbSe_2$, Phys. Rev. B **16**, 801 (1977).

[41] H. Lin, W. Huang, K. Zhao, C. Lian, W. Duan, X. Chen, and S.-H. Ji, Growth of atomically thick transition metal sulfide films on graphene/6H-SiC(0001) by molecular beam epitaxy, Nano Res. **11**, 4722 (2018).

[42] R. Bianco, I. Errea, L. Monacelli, M. Calandra, and F. Mauri, Quantum enhancement of charge density wave in NbS_2 in the two-dimensional limit, Nano Lett. **19**, 3098 (2019).

[43] G. Wexler and A. M. Woolley, Fermi surfaces and band structures of the 2H metallic transition-metal dichalcogenides, J. Phys. C **9**, 1185 (1976).

[44] J. A. Wilson, Charge-density waves in the 2H-$TaSe_2$ family: Action on the Fermi surface, Phys. Rev. B **15**, 5748 (1977).

[45] A. H. Castro Neto, Charge density wave, superconductivity, and anomalous metallic behavior in 2D transition metal dichalcogenides, Phys. Rev. Lett. **86**, 4382 (2001).

[46] D. S. Inosov, V. B. Zabolotnyy, D. V. Evtushinsky, A. A. Kordyuk, B. Buchner, R. Follath, H. Berger, and S. V. Borisenko, Fermi surface nesting in several transition metal dichalcogenides, New J. Phys. **10**, 125027 (2008).

[47] J. Laverock, D. Newby, Jr., E. Abreu, R. Averitt, K. E. Smith, R. P. Singh, G. Balakrishnan, J. Adell, and T. Balasubramanian, $\boldsymbol{k}$-resolved susceptibility function of 2H-$TaSe_2$ from angle-resolved photoemission, Phys. Rev. B **88**, 035108 (2013).

[48] See Supplemental Material at http://link.aps.org/supplemental/10.1103/PhysRevResearch.6.013088 for the discussion of (i) the ARPES measurements (including measurement geometry, data symmetrization process, and impact of polarization of the incoming photons) and (ii) potassium deposition, (iii) comments on our attempts to study the 2H-$TaSe_2$ surface using scanning transmission microscopy, (iv) low-energy electron diffraction investigations of the 2H-$TaSe_2$ surface upon potassium doping, (v) importance of the out-of-plane dispersion, (vi) establishing the occurrence of the Lifshitz transition in our system, (vii) comparison of the symmetry of ARPES features around $\boldsymbol{K}$ in pristine and highly doped samples, (viii) simulation of spectral weights in the vicinity of $\boldsymbol{K}$ for the (3×3) and $(2\sqrt{3} \times 2\sqrt{3})R30^\circ$ phases, (ix) the saddle-point effective model for $\delta \neq 0$, (x) comparison of the impact of the (2×2) and $(2\sqrt{3} \times 2\sqrt{3})R30^\circ$ orders on the band structure in the vicinity of the saddle points, and (xi) comparison of the electronic density of states of the uncorrelated state and the (2×2) CDW.

[49] S. V. Borisenko, A. A. Kordyuk, A. N. Yaresko, V. B. Zabolotnyy, D. S. Inosov, R. Schuster, B. Buchner, R. Weber, R. Follath, L. Patthey, and H. Berger, Pseudogap and charge density waves in two dimensions, Phys. Rev. Lett. **100**, 196402 (2008).

[50] J. M. Riley, F. Mazzola, M. Dendzik, M. Michiardi, T. Takayama, L. Bawden, C. Granerod, M. Leandersson, T. Balasubramanian, M. Hoesch, T. K. Kim, H. Takagi, W. Meevasana, Ph. Hofmann, M. S. Bahramy, J. W. Wells, and P. D. C. King, Direct observation of spin-polarized bulk bands in an inversion-symmetric semiconductor, Nat. Phys. **10**, 835 (2014).

[51] S. Beaulieu, J. Schusser, S. Dong, M. Schuler, T. Pincelli, M. Dendzik, J. Maklar, A. Neef, H. Ebert, K. Hricovini, M. Wolf, J. Braun, L. Rettig, J. Minar, and R. Ernstorfer, Revealing hidden orbital pseudospin texture with time-reversal dichroism in photoelectron angular distributions, Phys. Rev. Lett. **125**, 216404 (2020).

[52] P. D. C. King, S. Picozzi, R. G. Egdell, and G. Panaccione, Angle, spin, and depth resolved photoelectron spectroscopy on quantum materials, Chem. Rev. **121**, 2816 (2021).

[53] J.-A. Yan, M. A. Dela Cruz, B. Cook, and K. Varga, Structural, electronic and vibrational properties of few-layer 2H- and 1T-$TaSe_2$, Sci. Rep. **5**, 16646 (2015).

[54] M. P. Seah and W. A. Dench, Quantitative electron spectroscopy of surfaces: A standard data base for electron inelastic mean free paths in solids, Surf. Interface Anal. **1**, 2 (1979).

[55] D. S. Inosov, D. V. Evtushinsky, V. B. Zabolotnyy, A. A. Kordyuk, B. Buchner, R. Follath, H. Berger, and S. V. Borisenko, Temperature-dependent Fermi surface of 2H-$TaSe_2$ driven by competing density wave order fluctuations, Phys. Rev. B **79**, 125112 (2009).

[56] N. V. Smith, S. D. Kevan, and F. J. DiSalvo, Band structures of the layer compounds 1T-TaS_2 and 2H-$TaSe_2$ in the presence of commensurate charge-density waves, J. Phys. C: Solid State Phys. **18**, 3175 (1985).

[57] C. M. Varma and W. Weber, Phonon dispersion in transition metals, Phys. Rev. Lett. **39**, 1094 (1977).

[58] C. M. Varma, E. I. Blount, P. Vashishta, and W. Weber, Electron-phonon interactions in transition metals, Phys. Rev. B **19**, 6130 (1979).

[59] F. Flicker and J. van Wezel, Charge order from orbital-dependent coupling evidenced by $NbSe_2$, Nat. Commun. **6**, 7034 (2015).

[60] F. Flicker and J. van Wezel, Charge order in $NbSe_2$, Phys. Rev. B **94**, 235135 (2016).

[61] C. Heil, H. Sormann, L. Boeri, M. Aichhorn, and W. von der Linden, Accurate bare susceptibilities from full-potential ab initio calculations, Phys. Rev. B **90**, 115143 (2014).

[62] R. L. Kurtz, D. A. Browne, and G. J. Mankey, Final state effects in photoemission studies of Fermi surfaces, J. Phys.: Condens. Matter **19**, 355001 (2007).

[63] A. Damascelli, Z. Hussain, and Z.-X. Shen, Angle-resolved photoemission studies of the cuprate superconductors, Rev. Mod. Phys. **75**, 473 (2003).

[64] V. N. Strocov, M. Kobayashi, X. Wang, L. L. Lev, J. Krempasky, V. V. Rogalev, T. Schmitt, C. Cancellieri, and M. L. Reinle-Schmitt, Soft-x-ray ARPES at the Swiss light source: From 3D materials to buried interfaces and impurities, Synchrotron Radiat. News **27**, 31 (2014).

[65] J. Hall, N. Ehlen, J. Berges, E. van Loon, C. van Efferen, C. Murray, M. Rosner, J. Li, B. V. Senkovskiy, M. Hell, M. Rolf, T. Heider, M. C. Asensio, J. Avila, L. Plucinski, T. Wehling, A. Gruneis, and T. Michely, Environmental control of charge density wave order in monolayer 2H-TaS_2, ACS Nano **13**, 10210 (2019).

[66] W. Wan, R. Harsh, P. Dreher, F. de Juan, and M. M. Ugeda, Superconducting dome by tuning through a van Hove singularity in a two-dimensional metal, npj 2D Mater Appl. **7**, 41 (2023).

[67] C. H. Chen, Electron diffraction study of the charge density wave superlattice in 2H-$NbSe_2$, Solid State Commun. **49**, 645 (1984).

[68] R. Rao, V. Carozo, Y. Wang, A. E. Islam, N. Perea-Lopez, K. Fujisawa, V. H. Crespi, M. Terrones, and B. Maruyama, Dynamics of cleaning, passivating and doping monolayer MoS_2 by controlled laser irradiation, 2D Mater. **6**, 045031 (2019).

[69] C. J. Sayers, L. S. Farrar, S. J. Bending, M. Cattelan, A. J. H. Jones, N. A. Fox, G. Kociok-Kohn, K. Koshmak, J. Laverock, L. Pasquali, and E. Da Como, Correlation between crystal purity and the charge density wave in 1T-VSe_2, Phys. Rev. Mater. **4**, 025002 (2020).

[70] S.-S. Chee, W.-J. Lee, Y.-R. Jo, M. K. Cho, D. Chun, H. Baik, B.-J. Kim, M.-H. Yoon, K. Lee, and M.-H. Ham, Atomic vacancy control and elemental substitution in a monolayer molybdenum disulfide for high performance optoelectronic device arrays, Adv. Funct. Mater. **30**, 1908147 (2020).

[71] A. König, K. Koepernik, R. Schuster, R. Kraus, M. Knupfer, B. Buchner, and H. Berger, Plasmon evolution and charge-density wave suppression in potassium intercalated 2H-$TaSe_2$, Europhys. Lett. **100**, 27002 (2012).

[72] M. K. Bin Subhan, A. Suleman, G. Moore, P. Phu, M. Hoesch, H. Kurebayashi, C. A. Howard, and S. R. Schofield, Charge density waves in electron-doped molybdenum disulfide, Nano Lett. **21**, 5516 (2021).

[73] D. Lin, S. Li, J. Wen, H. Berger, L. Forro, H. Zhou, S. Jia, T. Taniguchi, K. Watanabe, X. Xi, and M. S. Bahramy, Patterns and driving forces of dimensionality-dependent charge density waves in 2H-type transition metal dichalcogenides, Nat. Commun. **11**, 2406 (2020).

[74] X. Liu, Y. X. Chong, R. Sharma, and J. C. Seamus Davis, Discovery of a Cooper-pair density wave state in a transition-metal dichalcogenide, Science **372**, 1447 (2021).

[75] T. Kumakura, H. Tan, T. Handa, M. Morishita, and H. Fukuyama, Charge density waves and superconductivity in 2H-$TaSe_2$, Czech. J. Phys. **46**, 2611 (1996).

[76] J. Edwards and R. F. Frindt, Anisotropy in the resisitivity of $NbSe_2$, J. Phys. Chem. Solids **32**, 2217 (1971).

[77] D. M. Broun, What lies beneath the dome? Nat. Phys. **4**, 170 (2008).

[78] B. Michon, C. Girod, S. Badoux, J. Kacmarcik, Q. Ma, M. Dragomir, H. A. Dabkowska, B. D. Gaulin, J.-S. Zhou, S. Pyon, T. Takayama, H. Takagi, S. Verret, N. Doiron-Leyraud, C. Marcenat, L. Taillefer, and T. Klein, Thermodynamic signatures of quantum criticality in cuprate superconductors, Nature (London) **567**, 218 (2019).

[79] P. Giannozzi, O. Andreussi, T. Brumme, O. Bunau, M. Buongiorno Nardelli, M. Calandra, R. Car, C. Cavazzoni, D. Ceresoli, M. Cococcioni, N. Colonna, I. Carnimeo, A. Dal Corso, S. de Gironcoli, P. Delugas, R. A. DiStasio Jr., A. Ferretti, A. Floris, G. Fratesi, G. Fugallo *et al.*, Advanced capabilities for materials modelling with Quantum ESPRESSO, J. Phys.: Condens. Matter **29**, 465901 (2017).

[80] A. Dal Corso, Pseudopotentials periodic table: From H to Pu, Comput. Mater. Sci. **95**, 337 (2014).

[81] H. J. Monkhorst and J. D. Pack, Special points for Brillouin-zone integrations, Phys. Rev. B **13**, 5188 (1976).